Optimizing Electrode Placement Using Finite-Element Models in Radiofrequency Ablation Treatment Planning

Chun-Cheng R. Chen, Michael I. Miga, *Member, IEEE*, and Robert L. Galloway, Jr.*

Abstract—Conventional radiofrequency ablation (RFA) planning methods for identifying suitable electrode placements typically use geometric shapes to model ablation outcomes. A method is presented for searching electrode placements that couples finite-element models (FEMs) of RFA together with a novel optimization strategy. The method was designed to reduce the need for model solutions per local search step. The optimization strategy was tested against scenarios requiring single and multiple ablations. In particular, for a scenario requiring multiple ablations, a domain decomposition strategy was described to minimize the complexity of simultaneously searching multiple electrode placements. The effects of nearby vasculature on optimal electrode placement were also studied. Compared with geometric planning approaches, FEMs could potentially deliver electrode placement plans that provide more physically meaningful predictions of therapeutic outcomes.

Index Terms—Finite-element methods, optimization, radiofrequency ablation (RFA), treatment planning.

I. INTRODUCTION

FOCAL thermal ablative techniques have become widely adopted for the treatment of solid tumors. Examples include laser ablation [1], cryoablation [2], high-intensity focused ultrasound [3], and radiofrequency ablation (RFA) [4]. For ablation treatments to be successful, the extent of the ablated volume must overlap the detectable tumor volume entirely as well as a 1-cm surgical margin that contains possible occult disease. Although the physical mechanism of heat generation differs with each modality, the extent of the resulting ablation depends for all cases on the placement of the ablation device with respect to the targeted treatment volume. Consequently, controlling the placement of the device is a factor in producing successful ablative therapy.

The focus of this study is on the application of RFA in treating unresectable tumors of the liver. RFA works by inserting electrodes directly into a cancerous lesion. Radiofrequency currents (typically, 400–500 kHz) delivered through these electrodes produce resistive heating, and the resulting temperature increase causes focal thermal damage to the tissue. In a typical application of RFA, temperatures reach upward of 100 °C in the immediate areas around the active electrodes. Above a critical temperature (typically above 50 °C, for a duration of 2–5 min), tumors undergo coagulation necrosis, caused by irreversible cellular damage in the form of protein denaturation and disruption of cellular membranes. Cell death is considered instantaneous at around 60 °C [5]. In the course of an RFA treatment, the volume of ablated tissue increases as heat conduction distributes higher temperatures further into the tissue. In typical commercial RFA systems, a 3–5 cm spherical ablation zone is expected. Nevertheless, ablation of large tumors greater than 3 cm in diameter has proven to be less efficacious with incomplete ablation and subsequent local recurrence rates as high as 47.6% in one study [6]. Although multiple ablation strategies to create larger ablations have been employed clinically [7], the investigators cited a need for better intraoperative guidance as well as an appreciation of local physiological factors that affect ablation outcome.

Treatment planning of RFA device placement attempts to determine the position and orientation of the device relative to the targeted tissue that would maximize the therapeutic outcome as predicted by a model of RFA. At present, models of RFA used in treatment planning have largely relied upon geometric assumptions of the final ablation extents, typically spheres or ellipsoids [7]–[10]. The observed size and shape of RF ablations in clinical data, however, show significant variability in size and geometry [11], and simulation studies using computational models of RFA have demonstrated dependence of ablation extents on a number of physical parameters [12], [13]. These variations in ablation extents represent phenomena not readily predicted by geometric shapes. Further compounding this problem is the irregular distribution of thermal sinks in the liver, particularly vessels that are larger than 3 mm in diameter [14]. These vessels have been shown to remain patent during treatment, and their proximity to a treatment region reduces the local ablation extents. Consequently, variability in ablation volume and spatial extent is expected even within a single patient as the device is placed in different locations within the target organ. More recently, investigators have attempted to incorporate patient-specific anatomical information into planning, as well as propose methods for modifying the assumed ablation geometries in the presence of nearby vessels [9]. However, these methods are based on phenomenological approximations of the underlying physical processes, and thus make use of parameters that are not necessarily physically meaningful.

C.-C. R. Chen is with the Department of Biomedical Engineering, Vanderbilt University, Nashville, TN 37232 USA and also with Vanderbilt University School of Medicine (e-mail: richard.chen@vanderbilt.edu).

M. I. Miga and *R. L. Galloway, Jr. are with the Department of Biomedical Engineering, Vanderbilt University, Nashville, TN 37232 USA (e-mail: michael.i.miga@vanderbilt.edu; bob.galloway@vanderbilt.edu).
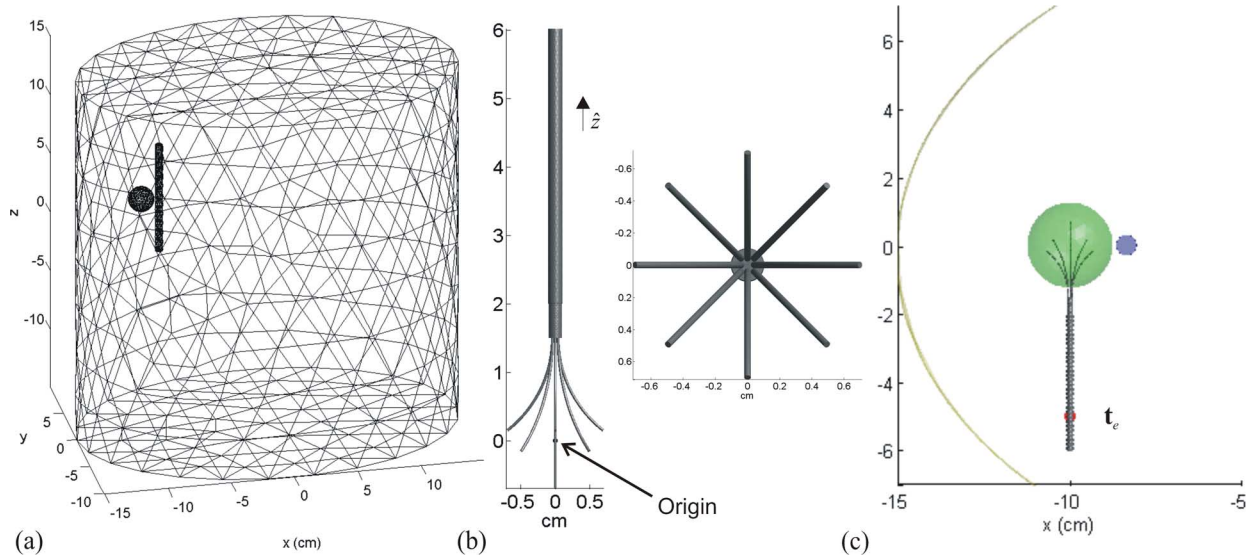
Fig. 1. (a) Wireframe model of the domain geometry in the global coordinate system. (b) Surface geometry of electrode model viewed in two projections in its local coordinate system. (c) Device, inserted through entry point located at $\mathbf{t}_e$, with tines embedded in spherical tumor, depicted with nearby vessel. The centroids of all three objects are on the $z = 5$ cm plane.

In this paper, a method is presented that uses finite-element models (FEMs) of RFA [15] to predict ablation outcomes for the purpose of planning electrode placement. Currently existing computational models of RFA are suitable only for evaluating static geometries with a fixed electrode position. The models will be extended to allow evaluations of multiple electrode placements via dynamic remeshing. Then, a strategy will be described to optimize the FEM predicted ablation result over the space of allowable electrode placements in a manner that minimizes the number of FEM evaluations.

II. METHODS

A. Finite-Element Model

The treatment domain and electrode geometries used in all simulation experiments are shown in Fig. 1. The electrode was modeled after the RITA Starburst XL RFA device (Rita Medical Systems, CA) in which the expandable electrodes have been deployed to the manufacturer's "2 cm" setting [Fig. 1(b)]. The positions of the tips of the nine tines were measured relative to the tip of the trocar housing the electrodes. Then, circular arcs were used as skeletons to connect the tine tips to the trocar tip. A circle 0.42 mm in diameter was extruded along the skeleton to generate the 3-D tines.

Each of the geometries has a local coordinate system. For the electrode, the origin was located 1.5 cm proximally from the tip of the center tine. The z-axis was defined to be parallel to the shaft of the electrode, and the y–z plane was arbitrarily chosen to contain one of the nine tines. In the treatment domain, the origin was located at the centroid of the outer cylinder representing the human torso. A spherical target volume was created. In simulation experiments, the target volume centroid was placed at coordinates $(-10 \text{ cm}, 0 \text{ cm}, 5 \text{ cm})$. If a spherical target volume was included in the model, it had a 2.5 cm diameter. In simulations involving vessels, a 6-mm cylinder running

parallel to the global z-axis was placed such that its centroid was at coordinates $(-8.6 \text{ cm}, 0 \text{ cm}, 5 \text{ cm})$ if no spherical target volume was present, or $(-8.35 \text{ cm}, 0 \text{ cm}, 5 \text{ cm})$ if there was a 2.5-cm spherical target volume.

The allowable electrode placements were constrained to simulate current RFA electrode placement techniques. The electrode was inserted through a prescribed entry point $\mathbf{t}_e$ [illustrated in Fig. 1(c)], with the goal of reaching a destination point after determining the correct trajectory. In all simulations, $\mathbf{t}_e$ was given the coordinates $(-10 \text{ cm}, -5 \text{ cm}, 5 \text{ cm})$. The depth of insertion and the orientation of the electrode relative to the entry point were then allowed to vary freely, giving only 4 DOF as all transformations applied to the electrode were assumed to be rigid about the origin of the electrode. Thus, for any point $\mathbf{x}$ given in the local coordinates of the electrode, the transformation $\mathcal{T}$ to the global coordinates of the domain is defined by

$$\mathbf{y} = \mathcal{T}(\mathbf{x}) = \mathbf{R}(\mathbf{x} - d\,\hat{\mathbf{z}}) + \mathbf{t}_e \qquad (1)$$

where d is the depth of insertion, $\hat{\mathbf{z}}$ corresponds to the axis of the electrode, and $\mathbf{R}$ is a rotation matrix parameterized by sequential rotations about the x-, y-, and z-axes of the domain [i.e., $\mathbf{R} = \mathbf{R}_x(\phi_x)\,\mathbf{R}_y(\phi_y)\,\mathbf{R}_z(\phi_z)$]. To simplify discussion, a parameter vector $\boldsymbol{\theta}$ is defined whose elements are d and the three Eulerian angles

$$\boldsymbol{\theta} = [d, \phi_x, \phi_y, \phi_z]. \qquad (2)$$

In all simulation experiments, the starting orientation and position was derived using $\boldsymbol{\theta}^* = [5.0 \text{ cm}, 90°, 0°, 0°]$, resulting in a configuration shown in Fig. 1.

For every new electrode position in which the FEM model needs to be evaluated, the entire domain is remeshed. A noncommercial meshing software package, Tetgen [16], was incorporated in order to generate volumetric meshes from an input surface mesh using constrained Delaunay tetrahedralization. This software was further modified to include routines for

TABLE I
LIST OF MATERIAL PROPERTIES USED IN RFA SIMULATION

Properties	Symbol (units)	Value	Ref.
Thermal conductivity (human liver)	k (W/cm·K)	5.12e-3	[19]
Density (human liver)	ρ (g/mL)	1.06	[19]
Heat capacity (human liver)	c (J/g·K)	3.6	[19]
Density (blood)	ρ_b (g/mL)	1.0e-3	[19]
Heat capacity (blood)	c_b (J/g·K)	4.18	[19]
Perfusion	w_b (mL/mL/s)	6.4e-3	[19]
Electrical conductivity (human liver)	σ_0 (mS/cm)	3.33e-3	[19]
	σ_1 (1/K)	0.02	[24]
Activation energy	ΔE_a (J)	6.28e5	[22]
Activation factor	A (s^{-1})	3.1e98	[22]

Values represent the initial properties used in the simulations.

repairing intersecting surface meshes that result, for instance, from the electrode penetrating other structures such as the outer boundaries of the domain or the internal spherical surface representing the treatment region. Typically, 200 000–250 000 tetrahedral elements were generated in discretizing the domain, and 40 000–50 000 nodes are required. Element sizes ranged from 10^{-13} to 10^2 cm^3 in size, with the most refinement in a region 3 cm in diameter around the center of the electrode, where the maximum allowable element size was 10^{-4} cm^3. This level of refinement was selected after mesh convergence studies demonstrated less than 1% change in modeled ablation volumes over subsequent refinements.

B. Model Equations

Computational models of thermal ablation usually solve Pennes bioheat equation to obtain the transient temperature fields as a result of a local heat source:

$$\rho c \frac{\partial T}{\partial t} = \nabla \cdot k \nabla T - h_b (T - T_a) + Q_{\mathrm{RF}} \qquad (3)$$

where Q_{RF} (in watts per centimeter square) is the heat source, T (in degrees Celsius) is the temperature, k (watts per centimeter·kelvin) is thermal conductivity, ρ (in grams per centimeter cube) is the tissue density, and c (in joules per gram·kelvin), is the heat capacity. The convective heat transfer coefficient h_b (in watts per centimeter cube·kelvin inverse) models the rate of perfusion in the tissue, as arterial blood enters the tissue at a given temperature T_a (in degrees Celsius), and is assumed to equilibrate immediately with the surrounding tissue. The convective coefficient h_b is defined to be $h_b = \rho_b c_b w_b$, where the subscript b indicates properties specific to blood, and w_b is the perfusion rate (in milliliters per milliliter·second inverse). All material coefficients are defined in Table I. The heat source Q_{RF} can be approximated by first solving the electrostatic problem with appropriate boundary conditions

$$\nabla \cdot (-\sigma \nabla \Phi) = 0 \qquad (4)$$

where σ (in siemens per centimeter) is the conductivity of the medium and Φ (in volts) is the electrostatic potential. Given Φ, the heat source is then estimated as the time-averaged power density generated by the resulting current: $Q_{\mathrm{RF}} = (P_{\mathrm{set}}/P_0)\sigma |\nabla \Phi|^2/2$, where P_0 is the input power resulting from 1.0 V applied to the electrode and P_{set} is the desired power setting. In order to solve the coupled partial differential equations, many investigators have employed the finite-element method [17]–[20]. FEM models for RFA typically solve the electrostatic problem over a single meshed domain that is shared with the thermal problem. A single mesh shared for both equations allows the estimated power deposition from the electrostatic equation to be coupled directly into the FEM formulation of the thermal problem without additional interpolation steps.

Boundary conditions were specified as follows. For the electrostatic problem, the outer surface except the bottom face was prescribed an insulative, no-flux condition. A constant 1.0-V Dirichlet condition was applied on the conductive electrodes, and ground was placed on the bottom face. The total power P_{set} was set to 20 W, and the entire ablation was run for 10 min, after which the power was set to 0 W for 5 min. For the thermal problem, the cylindrical outer surface was given an adiabatic, no-flux condition, whereas the top and bottom faces were preset to 37 °C. If a vessel was modeled, the vessel surface was also prescribed a constant temperature of 37 °C.

Finally, a measure of tissue damage accumulated over the course of the ablation is computed. A suitable metric is the Arrhenius damage index Ω, which has been previously employed by investigators [17], [21], [22] to predict the resulting thermal damage to the tissue. This paper uses the survival fraction ω, which is related to the damage index by $\omega = \exp(-\Omega)$. Its dependence on temperature over time is given by

$$\frac{\partial \omega(x,t)}{\partial t} = -A \exp\left(-\frac{\Delta E_a}{\mathrm{R} T(x,t)}\right) \omega(x,t) \qquad (5)$$

with the initial condition that $\omega(\mathbf{x}, t_0) = 1$. In (5), ΔE_a is the activation energy (in joules), A the activation factor (in per seconds), and R the universal gas constant. The Arrhenius survival fraction ω can be interpreted as the ratio of viable cells to total cells inside a region of space. Initially, when $\omega = 1$, the tissue is considered completely viable, and when $\omega \ll 1$, the tissue has undergone coagulation necrosis. In this paper, the threshold used to demarcate the onset of coagulation necrosis was set to $\omega_0 = e^{-1}$ or approximately 37%.

As suggested previously by other investigators [15], [17], [23], this model implements temperature-dependent electrical conductivity and perfusion to account for relevant property changes observed in clinical ablations. The electrical conductivity of ionic solutions increases at a rate of 2%/°C [24]. Thus, the conductivity of the phantom is modeled as $\sigma = \sigma_0(1 + \sigma_1(T - T_0))$, where the coefficients σ_0 and σ_1 are given in Table I, and T_0 is the baseline temperature. On the other hand, perfusion decreases as temperature rises because of coagulation of microvasculature. There is, however, no consensus model of how this behavior should be modeled. In this study, the perfusion was scaled linearly by the local Arrhenius survival fraction $h_b = h_{b0}\omega(\mathbf{x}, t)$, in a manner similar to that proposed in [22], [25], and [26]. The temperature dependence of other parameters was neglected because its inclusion in the

model would produce relatively small changes in the final temperature [27]. As the mesh was regenerated for each electrode placement, appropriate material properties were automatically assigned to each tetrahedral element.

In order to solve the system of equations, an external iterative solver package (PETSc, [28]) was used. The transient temperature solution was obtained over 15 min via a fully implicit time-stepping scheme with 15-s intervals. Temperature-dependent properties were updated by using the temperature distribution from the previous iteration. A constant power setting was imposed on the electrostatic problem. Although currently many clinical ablation scenarios use power schedules guided by constant-temperature feedback [29], a constant-power setting was chosen to simplify the complexity of the model to only those necessary dynamics that could potentially predict ablations in matching experimental conditions. At every time step, the electrostatic field was updated with the new conductivity properties. The resulting power density was then scaled so that the total power in the domain was 20.0 W. This setting was predetermined so that the maximum temperature in the domain at the end of ablation, 10 min after start of the simulation, did not greatly exceed $100\,^{\circ}$C, thus preventing significant changes in tissue properties that would deviate from the model. After 10 min of ablation, the applied power was set to zero. These model parameters were tested in a phantom study [30] and demonstrated to predict ablations suitably.

C. Optimization Algorithm

1) Objective Function: In this study, the objective was to minimize the predicted Arrhenius survival fraction ω in a weighted sense everywhere in the region of interest (ROI), at the end of the simulation

$$\mathcal{J} = \int_{\mathrm{ROI}} W(\mathbf{x})\,\omega(\mathbf{x}, t_f)\,d\mathbf{x} \tag{6}$$

in which the weighting term W is given to be

$$W(\mathbf{x}) = \begin{cases} 1, & \mathbf{x} \in \text{target volume} \\ 0, & \text{otherwise.} \end{cases} \tag{7}$$

The objective function as defined before represents the residual target volume that is viable after ablation. Minimizing $\mathcal{J}$ is tantamount to reducing the likelihood of local recurrence due to residual tumor cells within the target volume. The objective function defined in (6) is implicitly a function of the electrode parameters $\boldsymbol{\theta}$ since ω is dependent on the orientation and location of the electrode. In the computational experiments, the final survival fraction was recorded 5 min after power shut off, or at $t_f = 15$ min.

2) Search Method: In order to search for the electrode position that optimizes the given objective function, the resulting ablation zone for each electrode position needs to be computed. A straightforward implementation would reevaluate the FEM model for each new electrode position to recompute the objective function. Because constructing and solving the FEM model are computationally expensive processes, it is useful to develop a method that minimizes the number of FEM model reevaluations. In this study, the strategy was to approximate the resulting

Arrhenius solution ω as a field that transforms rigidly with the electrode, thus recasting the search as an image processing problem. Computationally, the objective function (6) can be viewed as the correlation of two scalar volumetric images. The first "image" W describes the relative importance of a point in the target domain in the objective. The second "image" ω represents the likelihood of achieving complete ablation at a given position relative to the electrode. Because ω is defined in terms of survivability, the optimal localization of the electrode is estimated by the parameters $\tilde{\boldsymbol{\theta}}$ that would transform the ω image to be minimally correlated with the W image

$$\tilde{\boldsymbol{\theta}} = \arg\min_{\boldsymbol{\theta}} \int_{\mathrm{ROI}} W(\mathbf{x})\,\omega(\hat{\mathcal{T}}(\mathbf{x}; \boldsymbol{\theta}), t_f)\,d\mathbf{x} \tag{8}$$

where $\hat{\mathcal{T}}$ is the incremental transformation from some initial position and orientation of the electrode $\boldsymbol{\theta}_0$, as given by

$$\hat{\mathcal{T}}(\boldsymbol{\theta}) = \mathcal{T}(\boldsymbol{\theta}) \circ \mathcal{T}^{-1}(\boldsymbol{\theta}_0) \tag{9}$$

and $\mathcal{T}$ was previously defined in (1).

The proposed strategy depends on the assumption that the ablation shape does not change significantly over small perturbations of its orientation and position. The justification comes from the observation that the RF power is deposited chiefly within a few millimeters [31] of the conductive electrodes, and in particular near the tips of the tines. Thus, the regions of highest power density tend to vary closely with the position and orientation of the electrode. If the domain is homogeneous and the relevant boundary conditions sufficiently far away, then the resulting ablation shape would be largely invariant with respect to the electrode position and orientation. Nevertheless, in clinically relevant applications such as in the liver, there is, in fact, local material inhomogeneity, and thermal and electrical boundary conditions may be nearby. Thus, some spatial variability of the ablation with respect to the electrode is expected as the electrode is relocated during the search process. To correct for deviations from assumptions in the image correlation problem, the FEM was reevaluated periodically to update ω.

The following steps were taken to implement this strategy. At iteration m of the global search loop, the survival distribution ω_m was obtained by reevaluating the FEM problem. Then, ω_m was sampled around the present orientation and position of the electrode to form a discrete image ω_m. The samples form a Cartesian grid of 1-mm cubic pixels spanning 6 cm each direction, a volume sufficiently large enough to capture the expected ablation extents. This "electrode" grid was axis-aligned with the local reference frame of the electrode and centered about the origin of the electrode. Sampling of the tetrahedral mesh at these transformed grid points required multiple point location queries, which were facilitated by construction of a search tree that sorted the tetrahedra of the meshed domain into rectangular bins.

A second set of pixels was used to sample the weighting function W defined over the ROI to generate the discrete image $\mathbf{W}$. These pixels from the "domain" grid were also sampled on a Cartesian grid of the same size as that of ω_m, but were axis-aligned to the global coordinates and centered on the region of interest. The algorithm then entered a local search, where at each

iteration n of the local search, a new set of placement parameters was determined in an attempt to minimize the discretized form of the objective function

$$\mathcal{J}_{m,n} = \sum_{\mathbf{x} \in \mathbf{W}} W(\mathbf{x}) \, \omega_m^I (\hat{\mathcal{T}}(\mathbf{x}; \boldsymbol{\theta}_n), t_f) \qquad (10)$$

where ω_m^I gives the trilinearly interpolated values of the image ω_m for transformed pixels of the weighting image $\mathbf{W}$ that do not fall on the grid points of ω_m. Specifically,

$$\omega^I(\mathbf{x}) = \sum_{i,j,k=\{0,1\}} \omega_{ijk}^I \eta_{ijk}(\mathbf{x}) \qquad (11)$$

where ω_{ijk}^I gives the eight sampled neighbors of $\boldsymbol{\omega}$ that form a bounding box around the point $\mathbf{x}$ and $\eta_{ijk}(\mathbf{x})$ is a trilinear interpolant with unit value at each vertex of the bounding box.

The optimization method for the image correlation was steepest descent [32]. The gradient of the objective function $\nabla_\theta \mathcal{J}$ was readily obtained analytically from (10) (see the Appendix). Termination of the local optimization was based on gradient magnitude and relative change in sequential values of $\mathcal{J}_{m,n}$. Also, the optimization was terminated after 1000 iterations of steepest descents. Upon termination of the image correlation step, the FEM model was reevaluated at the most recent value of $\boldsymbol{\theta}_n$. In this manner, multiple rounds of FEM evaluation and image correlation minimization were performed until the search obtained a solution $\boldsymbol{\theta}_f$.

3) Termination Criteria: The global search loop, which consisted of alternating rounds of image correlation minimization and FEM evaluation, was terminated upon reaching the maximum number of iterations prescribed. Experience with the algorithm suggested that typically no more than ten global search steps were required. The search was also stopped if the maximum displacement of all tine tips was less than 0.01 cm between subsequent steps. Finally, in order to prevent nonconvergent behavior (e.g., sequential steps that produced oscillatory objective function values), the search was terminated whenever the current function evaluation exceeded the previous function evaluation. This behavior occurred most often when the electrode placement was already near a local optimum, at which point numerical noise (e.g., from FEM discretization and sampling of the solution) was the major contributor to variations in the subsequent function evaluations. All algorithms were implemented in C++ on a Win32 platform using a 3.4-GHz Pentium IV processor with 2 GB of RAM. Run-time for a typical optimization for a single ablation was less than 2 h. The algorithm was automated to run without user intervention given inputs of a surface geometry, initial electrode placement, and model parameters.

III. SIMULATION EXPERIMENTS

A. Single Ablations

In order to test the robustness of the optimization algorithm, the following evaluation method was performed for two geometries, designated cases 1 and 2, in which the only difference between the cases is the presence of a 6-mm vessel in case 2. An ablation was initially simulated with the known electrode placement $\boldsymbol{\theta}^*$, as described in Section II, with the resulting

TABLE II
RESULTS OF SINGLE ABLATION EXPERIMENTS

Case	Vessel absent		Vessel present	
$\mathcal{J}(\boldsymbol{\theta}^*)$	0.43 cm³		0.40 cm³	
$\mathcal{J}(\boldsymbol{\theta}_0)$	4.9 cm³		4.2 cm³	
$\mathcal{J}(\boldsymbol{\theta}_f)$	0.65 cm³		0.36 cm³	
	$\boldsymbol{\theta}_0 - \boldsymbol{\theta}^*$	$\boldsymbol{\theta}_f - \boldsymbol{\theta}^*$	$\boldsymbol{\theta}_0 - \boldsymbol{\theta}^*$	$\boldsymbol{\theta}_f - \boldsymbol{\theta}^*$
Δd (mm)	5.0	-1.0e-3	5.0	3.7e-2
$\Delta\phi_x$	-9.57°	0.91°	-9.57°	0.10°
$\Delta\phi_y$	5.73°	0.86°	5.73°	0.21°
$\Delta\phi_z$	5.73°	4.34°	5.73°	8.10°
$E[|\Delta x_{tine}|]$	1.2 mm		0.91 mm	

ablation zone segmented using the ω_0 threshold. All of the points in this segmented ablation were designated to be the target volume. The known electrode placement was then perturbed from $\boldsymbol{\theta}^*$ along each of the 4 DOF by an amount given by $\boldsymbol{\theta}_0 - \boldsymbol{\theta}^*$ in Table II. The perturbations changed the average tine positions, $E[|\Delta x_{\text{tine}}|]$, in each case by 9.1 mm. Using the perturbed electrode placement $\boldsymbol{\theta}_0$ as an initial guess, the optimization algorithm was executed to determine an optimized placement $\boldsymbol{\theta}_f$ that would cover the target volume and attempt to recover the original, known electrode placement $\boldsymbol{\theta}^*$.

The optimization results for both cases were able to recover the original electrode position to within millimeter accuracy (0.9–1.2 mm), as measured by the average change in tine positions from the starting placement to the optimized placement. The algorithm also reported a lower objective function with the optimized position $\mathcal{J}(\boldsymbol{\theta}_f)$ than the value from the perturbed placement $\mathcal{J}(\boldsymbol{\theta}_0)$ with a value comparable to the unperturbed starting position $\mathcal{J}(\boldsymbol{\theta}^*)$ (see Table II). The result for case 1 (without the vessel) is shown in Fig. 2, where the optimization program was able to relocate the electrode so that the optimized ablation covered the initial ablated region. Despite this improvement, however, the result showed a slight asymmetry in coverage on the region surface, where one side was ablated more completely (i.e., lower values of ω) than the other. In ablation experiments where the optimization method was executed simply on the unperturbed electrode (results not shown), the optimizer also generated similar asymmetry in the final ablation, as is reported here. This result was likely due to numerical artifacts caused by sampling the FEM solution ω onto a Cartesian grid. Because the survival distribution transitions sharply between 0 and 1 in space, the sampling process could cause a misrepresentation of the local ablation at the margin, manifesting as noise in the objective function. This problem may be resolved by increasing the resolution of the sampling grid, or by postprocessing the sampled image ω, such as applying smoothing filters. Despite this sensitivity to sampling error, the results were still reasonable considering that this experiment represented worst-case scenarios in which the target volume was as large as the ablation. Furthermore, it was not a consistent error, as comparatively speaking, the scenario for case 2 (with a vessel present), shown in Fig. 3, produced
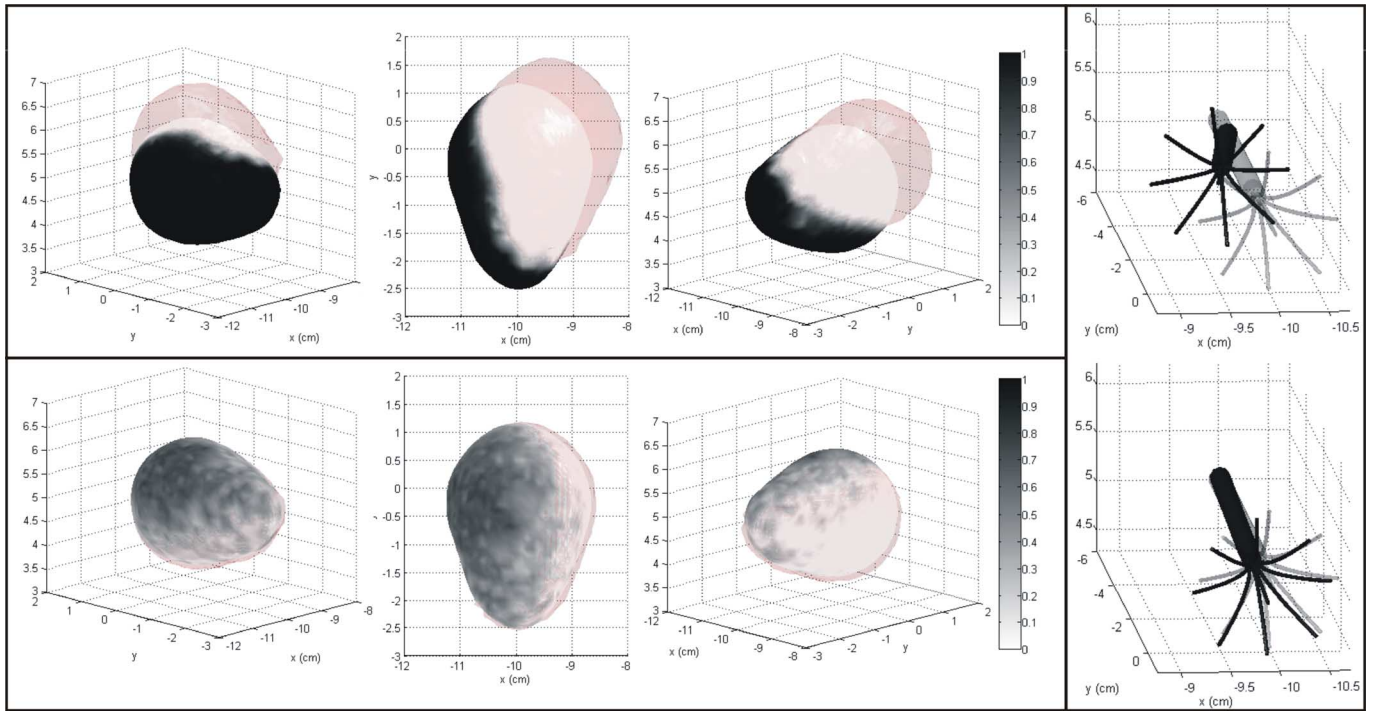
Fig. 2.   (Upper left panel) Ablations shown from left to right in lateral, superior, and medial views. The solid shape is the ablation from initial placement $\boldsymbol{\theta}^*$ and the translucent shape is the ablation from perturbed placement $\boldsymbol{\theta}_0$. Gray levels on surface correspond to values of ω, given by crossbar on the right. (Lower left panel) Results after optimization of electrode placement. The translucent shape is now from optimized placement $\boldsymbol{\theta}_f$. (Right panel) Comparison of electrode placement at $\boldsymbol{\theta}_0$ on the top and $\boldsymbol{\theta}_f$ on the bottom. The lightly shaded electrode is the original electrode placement $\boldsymbol{\theta}^*$.
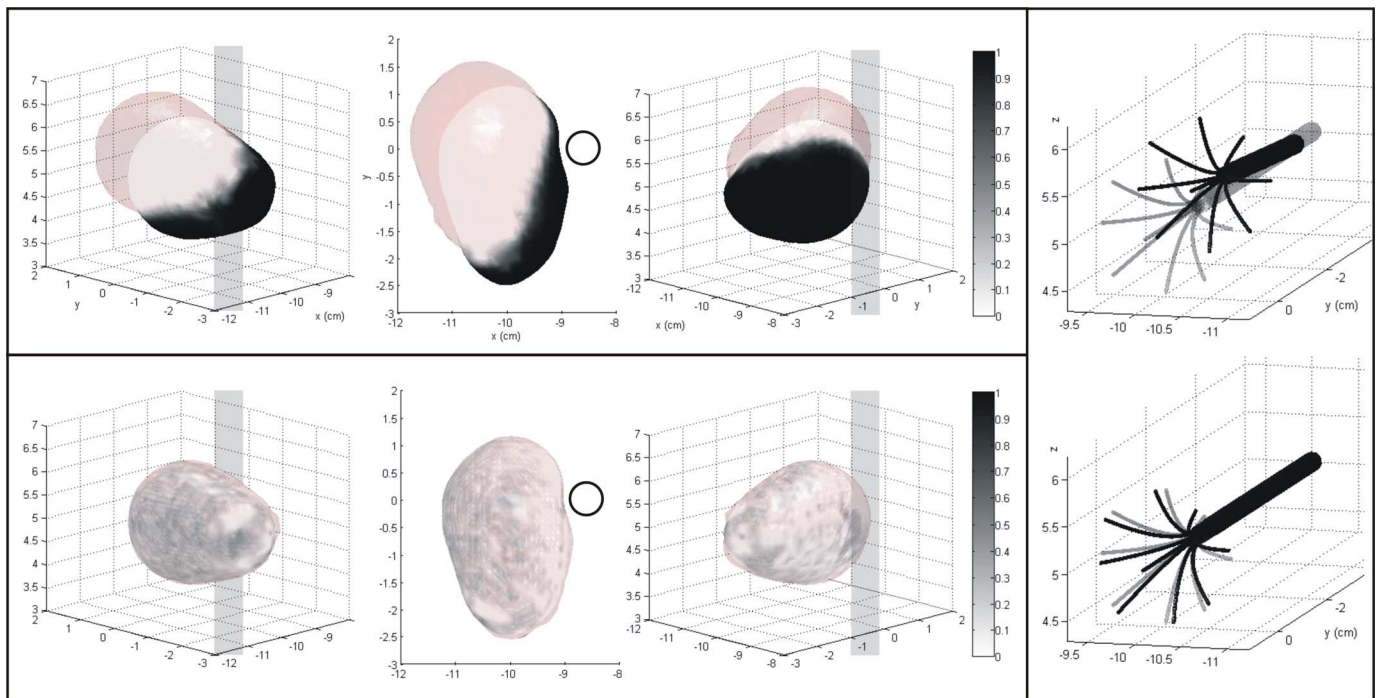

Fig. 3.   Same arrangement as in Fig. 2 except for the additional presence of a 6-mm vessel.
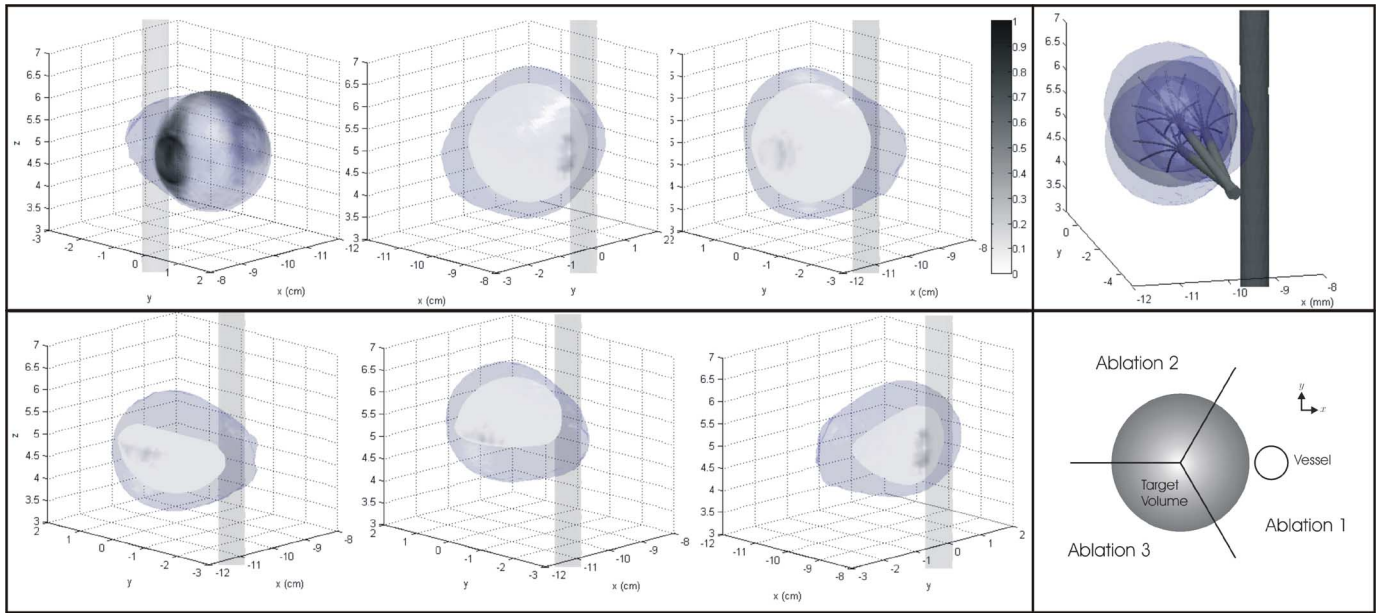
Fig. 4. (Upper left panel) Leftmost figure shows single ablation result as a surface map on the spherical target volume, rendered translucently to show nonablated areas (dark shade) seen around the periphery, particularly near the vertical vessel. In comparison, adjacent figures show results of optimized multiple ablations shown in lateral and medial views, with reduced nonablataed areas. Gray levels for surface shading correspond to the survival fraction ω, as depicted in the crossbar on the right. (Upper right panel) Optimized placements for each electrode. (Lower left panel) Results of multiple ablation planning for each wedge that correspond, going from right to left, to ablation 1–3, as labeled in the schematic on the (lower right panel).

a more homogeneous residual surface distribution than in case 1. The results also showed that ablations were fairly insensitive to rotation about the shaft of the device (i.e., ϕ_z). Consequently, the optimizer was generally unable to recover the original shaft roll.

B. Multiple Ablations

While using the same external geometry as in the single ablation experiments before, a 2.5-cm spherical treatment instead was placed 1 mm away from a 6-mm vessel. Although this treatment volume is small by clinical standards, it was chosen because the probe configuration had been previously evaluated in phantom against the model [30]. A 2.5-cm spherical target, 9.2 cm^3 in volume, was known to be comparable in size to the expected ablation using the given ablation probe geometry described before. Nevertheless, with optimal planning using a single ablation, there was nonablated regions on the periphery of the spherical target volume, as shown in Fig. 4. In order to plan multiple ablations, the treatment region was first decomposed into three equal sections, as depicted in the same figure. This step was achieved by k-means clustering [33] the treatment volume image using three seed points. One seed point was initialized to be close to the vessel so that the resulting partition would tend to maximize the number of image points close to the vessel. Electrode placement was then optimized independently for each section, and the resulting ablations were combined by multiplying the individual survival fractions (see the Appendix). Compared to the original single ablation, the results were markedly improved in which the predicted residual target volume was orders of magnitude smaller than for the sin-

TABLE III
RESULTS OF MULTIPLE ABLATION EXPERIMENT

	Ablation vol. (cm^3)	$\mathcal{J}(\boldsymbol{\theta}_0)$ (cm^3)	$\mathcal{J}(\boldsymbol{\theta}_f)$ (cm^3)	$E[|\Delta x_{tine}|]$ (mm)
Abl. 1	10.5	.27	6.4e-6	5.9
Abl. 2	12.1	.30	8.4e-4	3.8
Abl. 3	11.8	.40	1.8e-4	4.2
Combined	18.6	.97	2.5e-4	--
Single	11.9	.97	2.3e-1	--

gle ablation case. As listed in Table III, the combined ablations create an ablation that is nearly twice that of the target volume, and a 56% increase over the volume of the single ablation.

It should be noted that only three ablations were required to generate a larger ablation zone. In planning with geometric spheres, investigators previously noted that at least four ablation spheres were necessary to achieve an ablation of a spherical target volume larger than each ablation sphere [34]. The present result was possible because the predicted ablation geometry was shaped like a teardrop. Compared with a sphere, the teardrop shape was elongated along the axis of the RFA device and thus was capable of covering wedge-shaped sections as used in this experiment. Another notable observation was the net change in electrode placement to achieve the simulated outcome. In geometric planning that used spheres as ablation models, the plan would expect to place the electrodes symmetrically within a spherical target volume. In the results described before, however, the arrangement of electrodes was asymmetric, with the electrode ablating the section closest to the vessel being displaced furthest from the optimized single ablation placement

in the direction of the 6-mm vessel. The increase in displacement was needed to ablate the margin closest to the vessel, so that more power could be deposited near the vessel wall.

IV. DISCUSSION

In this paper, a method has been described to automate searches of optimal electrode placement for RFA. This technique potentially enhances the ability of clinicians to design patient-specific plans by using not only patient anatomy but also relevant parameters that are physically meaningful and predictive. The method builds off of the theoretical observation that over small perturbations to electrode parameters, the ablation shape varies slowly. Thus, an efficient search method can be developed by assuming that the ablation shape transforms rigidly with the RFA device. To account for real-world scenarios in which thermal and electrical boundary conditions affect ablation shape locally, the search routine is updated periodically by reevaluating the RFA model to obtain a more accurate representation of the ablation shape. In this manner, the RFA model continues to inform the search process, but the number of model evaluations is minimized. The results presented suggest that the method is capable of optimizing electrode placement.

A feature of the proposed optimization method is that it is independent of the specific FEM model used to predict the ablation outcome. Indeed, improvements can be made to the model to include a more detailed analysis of local blood flow [35] as well as microvasculature stasis to account for the heat sink effect of vasculature [26]. Although constant-temperature boundary conditions for vessels were used in this study, they do not represent true heat-transfer mechanics. Ultimately, to translate the model to clinical use, model validation is required, including measurements of relevant material properties, incorporation of patient-specific anatomy, and comparison of predicted ablation outcome given an electrode position with the final ablation extents, such as initial work presented in [30]. Especially for multiple ablations, in which irreversible property changes may occur between successive ablations, such validation may be used to evaluate the assumptions made in this study. Other commercial RFA electrodes may also be incorporated into the proposed search framework, along with the specific power control methods used in the design, since the method does not presume any *a priori* shape to the ablation. This search strategy could itself be integrated into larger search problems that include additional surgically relevant problems. For instance, although in the method described the entry point was fixed in the optimization scheme, it may also be incorporated into the planning problem, in order to identify, for instance, the best trajectory to avoid critical organs or intervening vasculature. Moreover, this study could potentially enhance the planning framework previously presented by other investigators [9]. Another manner of incorporating this study into existing literature is in the use of multiple ablation planning strategies [8], [34]. Planned placements using, for instance, geometric shapes may be further refined using this framework by decomposing the target volume in a manner proposed in this study. Because FEM models may be able to predict physical phenomena that are not actually captured by geometric

shapes, this framework can potentially be used to generate more efficient and accurate plans.

APPENDIX

A. Derivation of Objective Function Gradient

To aid the optimization of the image alignment, an analytic derivative is derived for the objective function in (10). To simplify the notation, the indices m, n are dropped; the variable $\mathbf{y}$ is assigned to be the transformed image coordinate $\mathbf{y} = \hat{\mathcal{T}}(\mathbf{x}; \boldsymbol{\theta}) = \mathcal{T}(\mathbf{x}; \boldsymbol{\theta}) \circ \mathcal{T}^{-1}(\mathbf{x}; \boldsymbol{\theta}_0)$, and the time variable t_f is dropped. Then, the derivative with respect to each of the four parameters is given by the chain rule

$$\frac{\partial}{\partial \theta_i} \mathcal{J} = \sum_{\mathbf{x} \in \mathbf{W}} W(\mathbf{x}) \left(\nabla_{\mathbf{y}} \omega^I \cdot \frac{\partial \mathbf{y}}{\partial \theta_i} \right). \tag{12}$$

The first derivative on the right-hand side is the derivative of the interpolated survival fraction image $\boldsymbol{\omega}$

$$\nabla_{\mathbf{y}} \omega^I = \sum_{i,j,k=\{0,1\}} \omega_{ijk}^I \nabla_{\mathbf{y}} \eta_{ijk}(\mathbf{y}) \tag{13}$$

and the second derivative on the right-hand side forms the derivative of $\mathbf{y}$ with respect to each parameter

$$\frac{\partial \mathbf{y}}{\partial \theta_i} = \frac{\partial}{\partial \theta_i} \left(\mathbf{R} \left(\mathcal{T}^{-1}(\mathbf{x}; \boldsymbol{\theta}_0) - d\,\hat{\mathbf{z}} \right) + \mathbf{t}_e \right). \tag{14}$$

For the Euler angles and depth, the respective derivatives are

$$\frac{\partial \mathbf{y}}{\partial \phi_i} = \frac{\partial \mathbf{R}}{\partial \phi_i} \left(\mathcal{T}^{-1}(\mathbf{x}; \boldsymbol{\theta}_0) - d\hat{\mathbf{z}} \right) \qquad \frac{\partial \mathbf{y}}{\partial d} = -\mathbf{R}\hat{\mathbf{z}} \tag{15}$$

where

$$\frac{d}{d\phi_i} \mathbf{R}_i(\phi_i) = \mathbf{R}_i \left(\phi_i + \frac{\pi}{2} \right). \tag{16}$$

B. Arrhenius Solutions for Multiple Ablations

The Arrhenius damage index takes into account the whole thermal history of a multiple ablation treatment by integrating the damage for each ablation over time. Thus, over N ablations starting at t_0 and ending at t_f, the cumulative damage index is

$$\Omega = \int_{t_0}^{t_f} A e^{-\Delta E_a / \mathrm{RT}} dt = \sum_{i=0}^{N-1} \int_{t_i}^{t_{i+1}} A e^{-\Delta E_a / \mathrm{RT}} dt$$

$$= \sum_{i=0}^{N-1} \Omega_i \tag{17}$$

where the ith ablation occurs over the interval t_i to t_{i+1}, and produces a net damage index Ω_i. Because $\omega = \exp(-\Omega)$, the total survival fraction over multiple ablations is given by $\omega = \prod_{i=0}^{N-1} \omega_i$.

into this paper as well as sharing FEM and visualization software. They also wish to acknowledge the constructive criticisms of the anonymous reviewers, which have improved the document.

REFERENCES

[1] C. M. Pacella, G. Bizzarri, F. Magnolfi, P. Cecconi, B. Caspani, V. Anelli, A. Bianchini, D. Valle, S. Pacella, G. Manenti, and Z. Rossi, "Laser thermal ablation in the treatment of small hepatocellular carcinoma: Eesults in 74 patients," *Radiology*, vol. 221, pp. 712–720, 2001.

[2] T. K. Sotsky and T. S. Ravikumar, "Cryotherapy in the treatment of liver metastases from colorectal cancer," *Semin. Oncol.*, vol. 29, pp. 183–191, 2002.

[3] J. E. Kennedy, G. R. Ter Haar, and D. Cranston, "High intensity focused ultrasound: Surgery of the future?," *Br. J. Radiol.*, vol. 76, pp. 590–599, 2003.

[4] K. K. Ng and R. T. Poon, "Radiofrequency ablation for malignant liver tumor," *Surg. Oncol.*, vol. 14, pp. 41–52, 2005.

[5] S. N. Goldberg, "Radiofrequency tumor ablation: Principles and techniques," *Eur. J. Ultrasound*, vol. 13, pp. 129–147, 2001.

[6] T. Livraghi, S. N. Goldberg, S. Lazzaroni, F. Meloni, T. Ierace, L. Solbiati, and G. S. Gazelle, "Hepatocellular carcinoma: Radio-frequency ablation of medium and large lesions," *Radiology*, vol. 214, pp. 761–768, 2000.

[7] M. H. Chen, W. Yang, K. Yan, M. W. Zou, L. Solbiati, J. B. Liu, and Y. Dai, "Large liver tumors: Protocol for radiofrequency ablation and its clinical application in 110 patients–mathematic model, overlapping mode, and electrode placement process," *Radiology*, vol. 232, pp. 260–271, 2004.

[8] G. D. Dodd, IIIrd, M. S. Frank, M. Aribandi, S. Chopra, and K. N. Chintapalli, "Radiofrequency thermal ablation: Computer analysis of the size of the thermal injury created by overlapping ablations," *Am. J. Roentgenol.*, vol. 177, pp. 777–782, 2001.

[9] C. Villard, L. Soler, and A. Gangi, "Radiofrequency ablation of hepatic tumors: Simulation, planning, and contribution of virtual reality and haptics," *Comput. Meth. Biomech. Biomed. Eng.*, vol. 8, pp. 215–227, 2005.

[10] T. Butz, S. K. Warfield, K. Tuncali, S. G. Silverman, E. van Sonnenberg, F. A. Jolesz, and R. Kikinis, "Pre- and intra-operative planning and simulation of percutaneous tumor ablation," in *Proc. Med. Image Comput. Comput.-Assisted Intervention—MICCAI 2000* (Lecture Notes in Computer Science), 2000, vol. 1935, pp. 317–326.

[11] S. Mulier, Y. Ni, Y. Miao, A. Rosiere, A. Khoury, G. Marchal, and L. Michel, "Size and geometry of hepatic radiofrequency lesions," *Eur. J. Surg. Oncol.*, vol. 29, pp. 867–878, 2003.

[12] I. Chang, "Finite element analysis of hepatic radiofrequency ablation probes using temperature-dependent electrical conductivity," *Biomed. Eng. Online*, vol. 2, no. 12, 2003.

[13] D. Haemmerich, F. T. Lee, D. J. Schutt, L. A. Sampson, J. G. Webster, J. P. Fine, and D. M. Mahvi, "Large-volume radiofrequency ablation of ex vivo bovine liver with multiple cooled cluster electrodes," *Radiology*, vol. 234, pp. 563–568, 2005.

[14] D. S. Lu, S. S. Raman, P. Limanond, D. Aziz, J. Economou, R. Busuttil, and J. Sayre, "Influence of large peritumoral vessels on outcome of radiofrequency ablation of liver tumors," *J. Vasc. Interv. Radiol.*, vol. 14, pp. 1267–1274, 2003.

[15] E. J. Berjano, "Theoretical modeling for radiofrequency ablation: State-of-the-art and challenges for the future," *Biomed. Eng. Online*, vol. 5, no. 24, 2006.

[16] H. Si and K. Gaertner, "Meshing piecewise linear complexes by constrained delaunay tetrahedralizations," in *Proc. 14th Int. Meshing Roundtable*, San Diego, CA, Sep. 2005, pp. 147–164.

[17] I. A. Chang and U. D. Nguyen, "Thermal modeling of lesion growth with radiofrequency ablation devices," *Biomed. Eng. Online*, vol. 3, p. 27, 2004.

[18] D. Haemmerich, S. Tungjitkusolmun, S. T. Staelin, F. T. Lee, D. M. Mahvi, and J. G. Webster, "Finite-element analysis of hepatic multiple probe radio-frequency ablation," *IEEE Trans. Biomed. Eng.*, vol. 49, no. 8, pp. 836–842, Aug. 2002.

[19] S. Tungjitkusolmun, S. T. Staelin, D. Haemmerich, J. Z. Tsai, H. Cao, J. G. Webster, F. T. Lee, D. M. Mahvi, and V. R. Vorperian, "Three-dimensional finite-element analyses for radio-frequency hepatic tumor ablation," *IEEE Trans. Biomed. Eng.*, vol. 49, no. 1, pp. 3–9, Jan. 2002.

[20] T. P. Ryan and S. H. Goldberg, "Comparison of simulation and experimental results for RF thermal treatment devices with or without cooling," in *Proc. Therm. Treat. Tissue Image Guid.*, San Jose, CA, Jan. 1999, vol. 3594, pp. 14–25.

[21] W. C. Lin, C. Buttemere, and A. Mahadevan-Jansen, "Effect of thermal damage on the in vitro optical and fluorescence characteristics of liver tissue's," *IEEE J. Sel. Topics Quantum Electron.*, vol. 9, no. 2, pp. 162–170, Mar./Apr. 2003.

[22] H. J. Schwarzmaier, I. V. Yaroslavsky, A. N. Yaroslavsky, V. Fiedler, F. Ulrich, and T. Kahn, "Treatment planning for MRI-guided laser-induced interstitial thermotherapy of brain tumors–the role of blood perfusion," *J. Magn. Reson. Imag.*, vol. 8, pp. 121–127, 1998.

[23] L. J. Hayes, K. R. Diller, J. A. Pearce, M. R. Schick, and D. P. Colvin, "Prediction of transient temperature fields and cumulative tissue destruction for radio frequency heating of a tumor," *Med. Phys.*, vol. 12, pp. 684–692, 1985.

[24] R. Pethig and D. B. Kell, "The passive electrical properties of biological systems: Their significance in physiology, biophysics and biotechnology," *Phys. Med. Biol.*, vol. 32, pp. 933–970, 1987.

[25] B. M. Kim, S. L. Jacques, S. Rastegar, S. Thomsen, and M. Motamedi, "Nonlinear finite-element analysis of the role of dynamic changes in blood perfusion and optical properties in laser coagulation of tissue," *IEEE J. Sel. Topics Quantum Electron.*, vol. 2, no. 4, pp. 922–933, Dec. 1996.

[26] X. He, S. McGee, J. E. Coad, F. Schmidlin, P. A. Iaizzo, D. J. Swanlund, S. Kluge, E. Rudie, and J. C. Bischof, "Investigation of the thermal and tissue injury behaviour in microwave thermal therapy using a porcine kidney model," *Int. J. Hyperthermia*, vol. 20, pp. 567–593, 2004.

[27] A. V. Shahidi and P. Savard, "A finite element model for radiofrequency ablation of the myocardium," *IEEE Trans. Biomed. Eng.*, vol. 41, no. 10, pp. 963–968, Oct. 1994.

[28] S. Balay, K. Buschelman, W. D. Gropp, D. Kaushik, M. G. Knepley, L. C. McInnes, B. F. Smith, and H. Zhang, "PETSc," 2.3.0 ed., Argonne National Laboratory, Chicago, IL, 2005.

[29] D. Haemmerich and J. G. Webster, "Automatic control of finite element models for temperature-controlled radiofrequency ablation," *Biomed. Eng. Online*, vol. 4, no. 42, 2005.

[30] C. C. Chen, M. I. Miga, and R. L. Galloway, "Characterization of tracked radiofrequency ablation in phantom," *Med. Phys.*, vol. 34, pp. 4030–4040, 2007.

[31] D. Haemmerich, T. Staelin, S. Tungjitkusolmun, F. T. Lee, Jr., D. M. Mahvi, and J. G. Webster, "Hepatic bipolar radio-frequency ablation between separated multiprong electrodes," *IEEE Trans. Biomed. Eng.*, vol. 48, no. 10, pp. 1145–1152, Oct. 2001.

[32] R. Fletcher, *Practical Methods of Optimization*, 2nd ed. Chichester, NY: Wiley, 1987.

[33] T. Kanungo, D. M. Mount, N. S. Netanyahu, C. D. Piatko, R. Silverman, and A. Y. Wu, "An efficient k-means clustering algorithm: Analysis and implementation," *IEEE Trans. Pattern Anal. Mach. Intell.*, vol. 24, no. 7, pp. 881–892, Jul. 2002.

[34] Y. S. Khajanchee, D. Streeter, L. L. Swanstrom, and P. D. Hansen, "A mathematical model for preoperative planning of radiofrequency ablation of hepatic tumors," *Surg. Endosc.*, vol. 18, pp. 696–701, 2004.

[35] T. W. Sheu, C. W. Chou, S. F. Tsai, and P. C. Liang, "Three-dimensional analysis for radio-frequency ablation of liver tumor with blood perfusion effect," *Comput. Meth. Biomech. Biomed. Eng.*, vol. 8, pp. 229–240, 2005.

Authors' photographs and biographies not available at the time of publication.